ACS APPLIED MATERIALS & INTERFACES

Research Article

www.acsami.org

Comparison of $LiVPO_4F$ to $Li_4Ti_5O_{12}$ as Anode Materials for Lithium-Ion Batteries

Rui Ma, Lianyi Shao, Kaiqiang Wu, Miao Shui, Dongjie Wang, Jianguo Pan, Nengbing Long, Yuanlong Ren, and Jie Shu*

Faculty of Materials Science and Chemical Engineering, Ningbo University, Ningbo 315211, Zhejiang Province, People's Republic of China

Supporting Information

ABSTRACT: In this paper, we reported on a comparison of $LiVPO_4F$ to $Li_4Ti_5O_{12}$ as anode materials for lithium-ion batteries. Combined with powder X-ray diffraction, scanning electron microscopy, high-resolution transmission electron microscopy, galvanostatic discharge/charge tests and in situ X-ray diffraction technologies, we explore and compare the insertion/extraction mechanisms of $LiVPO_4F$ based on the $V^{3+}/V^{2+}/V^{+}$ redox couples and $Li_4Ti_5O_{12}$ based on the Ti^{4+}/Ti^{3+} redox couple cycled in 1.0−3.0 V and 0.0−3.0 V. The electrochemical results indicate that both $LiVPO_4F$ and $Li_4Ti_5O_{12}$ are solid electrolyte interphase free materials in 1.0−3.0 V. The insertion/extraction mechanisms of $LiVPO_4F$ and $Li_4Ti_5O_{12}$ are similar with each other in 1.0−3.0 V as proved by in situ X-ray diffraction. It also demonstrates that both samples possess stable structure in 0.0−3.0 V. Additionally, the electrochemical performance tests of $LiVPO_4F$ and $Li_4Ti_5O_{12}$ indicate that both samples cycled in 0.0−3.0 V exhibit much higher capacities than those cycled in 1.0−3.0 V but display worse cycle performance. The rate performance of $Li_4Ti_5O_{12}$ far exceeds that of $LiVPO_4F$ in the same electrochemical potential window. In particular, the capacity retention of $Li_4Ti_5O_{12}$ cycled in 1.0−3.0 V is as high as 98.2% after 20 cycles. By contrast, $Li_4Ti_5O_{12}$ is expected to be a candidate anode material considering its high working potential, structural zero-strain property, and excellent cycle stability and rate performance.

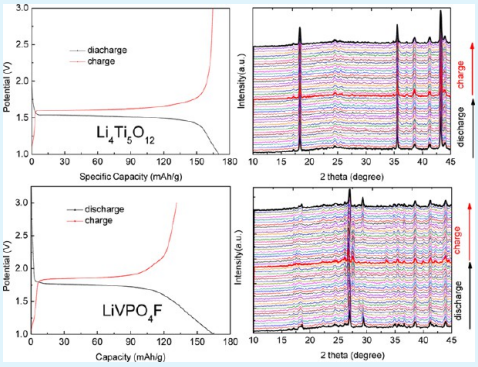

KEYWORDS: *$LiVPO_4F$, $Li_4Ti_5O_{12}$, anode materials, lithium-ion batteries, in situ X-ray diffraction*

1. INTRODUCTION

Lithium-ion batteries, as the preferred energy storage medium, are widely used in ranging from portable electronic products to large hybrid electric vehicles (HEVs) and electric vehicles (EVs) because of their high operating potential, superior energy density, excellent cycle lifetime, low raw material cost, environmental friendliness, and so forth.[1−4] Recently, the safety issue of lithium-ion batteries has increasingly attracted peoples' attentions. As conventional anode materials, commercial carbonaceous materials (especially graphite) could not satisfy the requirement under some special abuse conditions. At full charge, the low operating potential of highly lithiated graphite (LiC_6) electrode is close to the potential for metallic lithium deposition, which caused the growth of dendritic lithium on the surface of the anode, incurred obvious safety concerns, and limited the application in high-powder equipment.[5,6]

$Li_4Ti_5O_{12}$ owning high operating potential at 1.55 V, which has been already reported by many authors,[7−10] is a potential candidate as anode material for lithium-ion batteries due to its structural stability (zero-strain insertion material).[11] The structure of the spinel $Li_4Ti_5O_{12}$ belongs to the $Fd\bar{3}m$ space group, where some lithium ions are located at tetrahedral (8a) sites, and octahedral (16d) sites are occupied by another part of lithium ions and all the titanium ions with the atomic ratio of 1:5, and oxygen ions are located at 32e sites. Consequently, $Li_4Ti_5O_{12}$ can be described as $Li_{3(8a)}[LiTi_5]_{(16d)}O_{12(32e)}$. During insertion process, three lithium ions first occupy 16c sites, and simultaneously the lithium ions located at 8a sites in $Li_4Ti_5O_{12}$ also migrate to 16c sites, and then all 16c sites are occupied by lithium ions corresponding to the formation of rock-salt phase $Li_7Ti_5O_{12}$ ($Li_{3(8a)}[LiTi_5]_{(16d)}O_{12(32e)}$).

Although $LiVPO_4F$ was always used as cathode material based on the V^{3+}/V^{4+} redox couple in the previous studies, an additional lithium insertion reaction at around 1.8 V associated with the V^{2+}/V^{3+} redox couple in $LiVPO_4F$ was also reported by several recent investigations,[12−14] which allowed $LiVPO_4F$ as a potential anode material as well as a promising cathode in lithium-ion batteries.

To the best of our knowledge, anode materials are overcharged (<1.0 V) at the condition of short circuit or abuse. Consequently, it is essential to study the overcharge behaviors of anode electrodes at low potential, which will give the guidance to the additional lithium-ion insertion phenomena during overcharge under practical abuse. Until now, no detailed comparison of

Received: June 3, 2013
Accepted: August 8, 2013
Published: August 8, 2013

   dx.doi.org/10.1021/am402132u | ACS Appl. Mater. Interfaces 2013, 5, 8615−8627

$LiVPO_4F$ to $Li_4Ti_5O_{12}$ as anode materials for lithium-ion batteries has been reported. In this paper, we make a detailed research on the insertion/extraction mechanisms of $LiVPO_4F$ and $Li_4Ti_5O_{12}$ as anode materials for lithium ions batteries in a normal potential range 1.0−3.0 V and a broader electrochemical window (0.0−3.0 V) with in situ X-ray diffraction technology.

2. EXPERIMENTAL SECTION

2.1. Synthesis of $LiVPO_4F$ and $Li_4Ti_5O_{12}$ Samples. The preparation process of $LiVPO_4F$ is similar with that of the one reported by Barker.[15] First, a stoichiometric amount of V_2O_5 (AR, ≥99.0%), $NH_4H_2PO_4$ (AR, ≥99.0%) and acetylene black (25% mass excess) were mixed and sintered to yield the intermediate phase VPO_4, and then LiF was added to obtain the original material $LiVPO_4F$. Its detailed synthetic steps were reported in our previous paper.[16]

$Li_4Ti_5O_{12}$ was synthesized by a solid-state reaction. A stoichiometric amount of TiO_2 (AR ≥ 99.0%) and Li_2CO_3 (AR ≥ 98.0%) (2.5% mass excess) was mixed in a planetary ball-milling machine for 4 h and then sintered at 850 °C for 24 h in tubular furnace in an air atmosphere to avoid the formation of undesirable oxygen defect. Excess Li was provided to compensate for lithium volatilization during the high temperature reaction. The synthetic reaction is described as the following equation

$$2Li_2CCO_3 + 5TiO_2 \rightarrow Li_4Ti_5O_{12} + 2CO_2 \quad (1)$$

2.2. Electrode Preparation and Cell Assembling. The working electrode was prepared by mixing 60 wt % active material ($LiVPO_4F$ or $Li_4Ti_5O_{12}$), and 10 wt % polyvinylidene fluoride as adhesives and 30 wt % conductive carbon black. This powder mixture was manually ground and then dissolved in N-methylpyrodine to form homogeneous slurry, and then the slurry was coated on Cu foil, dried at 120 °C for 12 h in a vacuum oven, and cut into discs with a diameter of 15 mm. The counter electrode is Li metal. The separator is Whatman glass fiber diaphragm. The electrolyte is 1 mol/L $LiPF_6$ dissolved in a mixture of ethylene carbonate and dimethyl carbonate (1:1, v/v).

2.3. Analytical Methods. The powder X-ray diffraction patterns of $LiVPO_4F$ and $Li_4Ti_5O_{12}$ were collected on a Bruker D8 Focus diffractometer (40 kV, 40 mA), using Cu−Kα radiation (1.5406 Å). The particle morphologies were observed with a LEO1530 scanning electron microscopy (SEM). The crystal structure of particles was observed with JEM-2010 high-resolution transmission electron microscopy (HRTEM).

The galvanostatic charge/discharge tests were performed on LAND CT2001A battery test system (Wuhan Jinnuo, China). Lithium-ion batteries assembled with $LiVPO_4F$ and $Li_4Ti_5O_{12}$ working electrodes were cycled in 1.0−3.0 V and 0.0−3.0 V at current densities of 10, 20, 40, 80, and 160 mA/g.

The insertion/extraction mechanisms of $LiVPO_4F$ and $Li_4Ti_5O_{12}$ were studied by in situ X-ray diffraction technique using the Bruker D8 Focus diffractometer as described above. Prior to the in situ X-ray diffraction tests, $LiVPO_4F$ and $Li_4Ti_5O_{12}$ were respectively mixed with carbon black and subsequently ground in agate mortar, and then ready for the following in situ X-ray diffraction tests. All the simulated cells and in situ cells were assembled in an argon-filled glovebox with relative humidity under 5 ppm.

The homemade in situ cell used in this work was designed based on the adjustment of in situ Raman cell reported by our group previous paper,[17,18] which is mainly made up of stainless steel chamber, beryllium disc, working electrode, separator, lithium disc, stainless steel disc and polytetrafluoroethylene sleeve. We prepared the working electrode by mixing dozens of milligrams active materials with carbon black in advance and directly put it on the beryllium window of the in situ cell, and then placed separator, lithium metal, stainless steel disc and electrolyte in turn in the in situ cell chamber. All the collected in situ X-ray diffraction data were analyzed using the FULLPROF program.

3. RESULTS AND DISCUSSION

3.1. XRD Characterization. Figure 1 shows the XRD patterns of $LiVPO_4F$ (a) and $Li_4Ti_5O_{12}$ (b). The Bragg peaks of

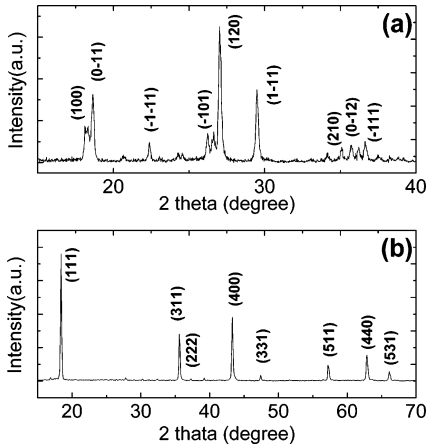

Figure 1. X-ray diffraction patterns of (a) $LiVPO_4F$ powder and (b)$Li_4Ti_5O_{12}$ powder.

the as-obtained $LiVPO_4F$, which are located at 18.2 18.6, 22.4, 26.3, 27.1, 29.5, 35.1, and 35.8° corresponding to the (100), (0−11), (−1−11), (−101), (120), (1−11), (210) and (0−12) planes, respectively, are in good accordance with those reported by Barker.[15] All the peaks can be indexed to JCPDS card No-22−1138 which belongs to the triclinic structure (space group P-1). The Rietveld refinement of XRD from phase $LiVPO_4F$ is carried out and the atomic positions are listed in Table S1 in the Supporting Information. However, we find few impurity of monoclinic-phase $Li_3V_2(PO_4)_3$ existing in $LiVPO_4F$ powder, which is induced by the sublimation loss of VF_3 during the preparative reaction.[19,20] As seen in Figure 1b, all the peaks of the pattern for $Li_4Ti_5O_{12}$ accord with JCPDS card No-26−1198. The Rietveld refinement of XRD from phase $Li_4Ti_5O_{12}$ is carried out and the atomic positions are listed in Table S2 in the Supporting Information. However, the weak diffraction peak at 27.5°is attributed to rutile TiO_2 impurity, which indicates the incomplete solid-state reaction at 850 °C with the transformation from anatase to rutile TiO_2 phase. The typical anatase to rutile TiO_2 phase transformation always takes place from 900 to 1000 °C. Because of the catalytic effect of Li_2CO_3,[6] rutile TiO_2 begins to form at 600 °C in the presence of Li_2CO_3. Besides this, all the obtained results of $Li_4Ti_5O_{12}$ are accordance with those reported previously.

3.2. Morphology Observation. The surface morphologies of $LiVPO_4F$ and $Li_4Ti_5O_{12}$ are observed by SEM technique as shown in images a and b in Figure 2, respectively. Figure 2a reveals that $LiVPO_4F$ powder has a uniform morphology with a

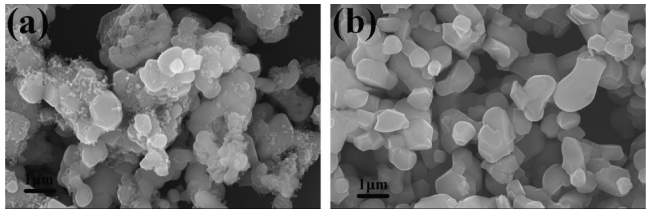

Figure 2. SEM images of (a) $LiVPO_4F$ powder and (b) $Li_4Ti_5O_{12}$ powder.

wide particle size distribution ranging from 0.5 to 2.0 μm. The presence of residual carbon black in $LiVPO_4F$ product, which could suppress the particles to aggregate and is beneficial to increasing the electronic conductivity, are observed. $Li_4Ti_5O_{12}$ powder has a relatively better uniform particle size distribution compared to that of $LiVPO_4F$ material, as shown in Figure 2b. The particle size of $Li_4Ti_5O_{12}$ is about 0.5 μm, which provides sufficient surface area between active materials and electrolyte, and enhances Li^+ diffusion coefficient in the electrode. To further confirm the existence of the residual carbon black, the HRTEM image of $LiVPO_4F$ powder is shown in Figure S1a, b in the Supporting Information. They present a nanosized (about 20–30 nm) conductive carbon network with a mean thickness of about 100 nm, which exists across the entire surface of active particles and connects all the active materials, and then minimizes the interparticle aggregation to improve the electrochemical property.[21] Because of too-thick $LiVPO_4F$ particles, we faild to observe the lattice of $LiVPO_4F$ in this experiment. In contrast, the fine crystal microstructure of $Li_4Ti_5O_{12}$ can be observed as shown in Figure S1c, d in the Supporting Information. The HRTEM image of $Li_4Ti_5O_{12}$ is composed of a highly crystalline phase, which indicates $Li_4Ti_5O_{12}$ is a well-crystallized sample.

3.3. Electrochemical and In Situ XRD Tests. Figure 3 shows the initial galvanostatic discharge/charge curves (a) and

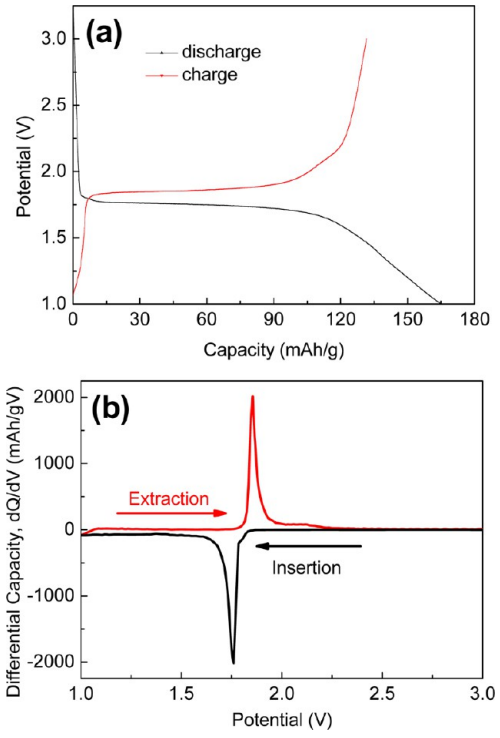

Figure 3. (a) Initial galvanostatic charge/discharge curves and (b) differential capacity profiles of $LiVPO_4F$ cycled in 1.0–3.0 V.

corresponding differential capacity profile (b) of $LiVPO_4F$ cycled at 10 mA/g in 1.0–3.0 V. It can be found that as-prepared $LiVPO_4F$ sample exhibits a lithiation plateau at 1.74 V during insertion and a reverse potential plateau at around 1.80 V during extraction, which is similar to the results reported by Barker,[12] Mba,[13,14] and Ellis[22] and indicates the reduction of $LiVPO_4F$ to Li_2VPO_4F via a two-phase process. This is different from the case of the reduction process of $LiFePO_4F$ or $LiFePO_4(OH)$ with half of the electrochemical curve exhibiting sloping behavior,[23,24] although they are all formed based on phosphate polyanion frameworks. Furthermore, the anode behaviors of $LiVPO_4F$ are quite different with those of $Li_3V_2(PO_4)_3$,[25] which appears in our prepared sample as trace impurity phase. The lattice mismatch between $LiVPO_4F$ and Li_2VPO_4F (space group $C2/c$) is the main reason for the flat electrochemical potential. On the basis of the reversibility of the V^{3+}/V^{2+} redox couple,[22] the lithium insertion/extraction reaction for $LiVPO_4F$ can be summarized as

$$LiV^{3+} + PO_4F + Li^+ + e^- \leftrightarrow Li_2V^{2+}PO_4F \quad (2)$$

On the basis of eq 2, a theoretical capacity of 156 mA h/g can be delivered corresponding to 1.0 Li uptake per formula. As shown in Figure 3a, the initial discharge capacity of $LiVPO_4F$ is just 156 mA h/g. It indicates that $LiVPO_4F$ totally transformed into $Li_2V^{2+}PO_4F$ after a discharge process to 1.0 V. However, the initial reversible charge capacity of $LiVPO_4F$ is 131.6 mA h/g in 1.0–3.0 V corresponding to $x = 0.84$ extraction from $Li_2V^{2+}PO_4F$ during recharge process, as shown in Figure 3a. Although trace $Li_3V_2(PO_4)_3$ appeared in our sample, the irreversible capacity of as-prepared $LiVPO_4F$ is not associated with the existence of $Li_3V_2(PO_4)_3$ because of its high-degree reversibility as anode material.[25] This is probably due to the occurrence of irreversible lithium insertion in the crystal structure of $LiVPO_4F$. The differential capacity profile of $LiVPO_4F$ in Figure 3b shows that the lithiation/delithiation process is also characterized by a couple of differential capacity peaks at around 1.76 and 1.81 V, which is in good agreement with the two-phase transformation reaction between $LiVPO_4F$ and Li_2VPO_4F.

To demonstrate the insertion/extraction behavior of Li/$LiVPO_4F$ battery, in situ XRD patterns were recorded and shown in Figure 4 and Figure S2 in the Supporting Information. Until now, no in situ XRD evolution of $LiVPO_4F$ as anode material has been reported. Here, a fully reversible two-phase reaction between the two end-number phases $LiVPO_4F$ and Li_2VPO_4F can be observed during the whole insertion/extraction process. When the lithium-ion is inserted into the sample, all the featured diffraction peaks of $LiVPO_4F$ gradually vanish and the Bragg positions of Li_2VPO_4F appears. During extraction, the featured diffraction peaks of Li_2VPO_4F disappear and the featured diffraction peaks of $LiVPO_4F$ reappear. These results are in accordance with the high-degree reversibility of the change in relative intensity vs 2 theta as the in situ XRD patterns illustrated in Figure 5. Consequently, the in situ XRD patterns clearly demonstrate the biphasic reaction mechanism between the two end-member phases $LiVPO_4F$ and Li_2VPO_4F, which is the same as the previous ex situ XRD results.[13] The volume change between $LiVPO_4F$ (174.337 Å^3) and Li_2VPO_4F (374.231 Å^3) is as large as 53.42% as shown in Table 1. Furthermore, the Rietveld refinement of XRD from phase $Li_4Ti_5O_{12}$ is carried out and the atomic positions are listed in Table S3 in the Supporting Information. On the basis of the XRD data, it can be found that the structure of Li_2VPO_4F is close to that of $LiVPO_4F$. Besides, it is also demonstrated by ex situ nuclear magnetic resonance that there are two distinct crystallographic sites for Li in the structure of Li_2VPO_4F.[26]

To closely compare of $Li_4Ti_5O_{12}$ to $LiVPO_4F$, Figure 6 illustrates the electrochemical property of $Li_4Ti_5O_{12}$ in the same potential window (1.0–3.0 V). $Li_4Ti_5O_{12}$ exhibits a flat potential plateau at around 1.55 V, which results from the coexistence of two phases of lithium titanates $Li_4Ti_5O_{12}$ and $Li_7Ti_5O_{12}$ caused by two-phase reaction between spinel and rock-salt phases

dx.doi.org/10.1021/am402132u | ACS Appl. Mater. Interfaces 2013, 5, 8615–8627

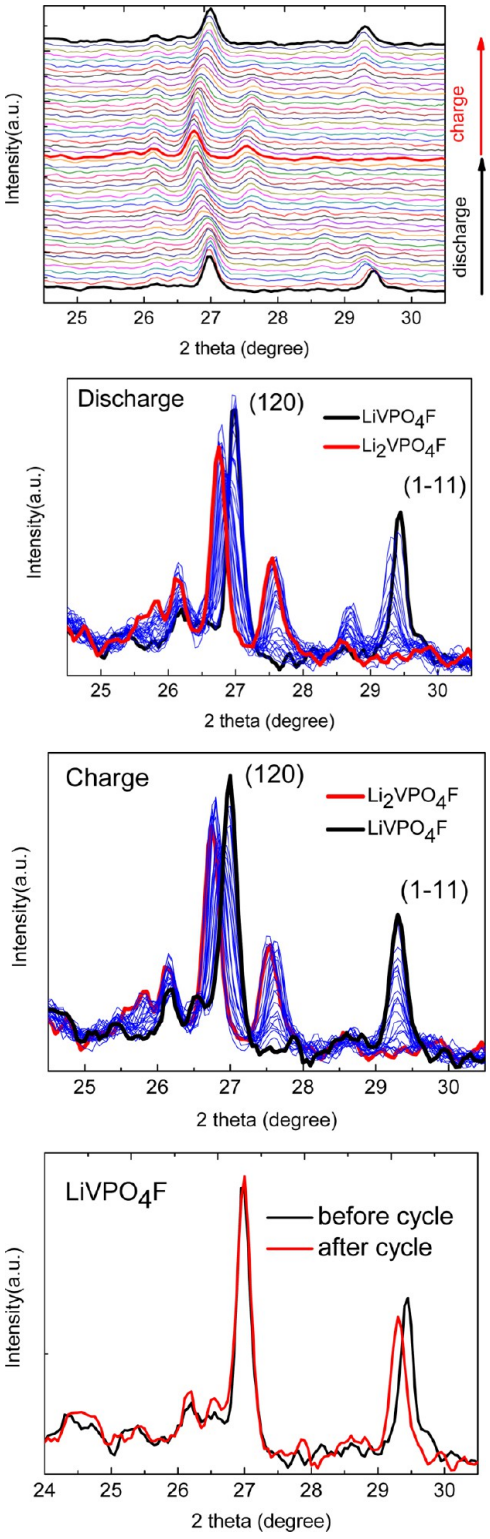

Figure 4. In situ XRD patterns during the first charge/discharge process of $LiVPO_4F$ cycled in 1.0−3.0 V.

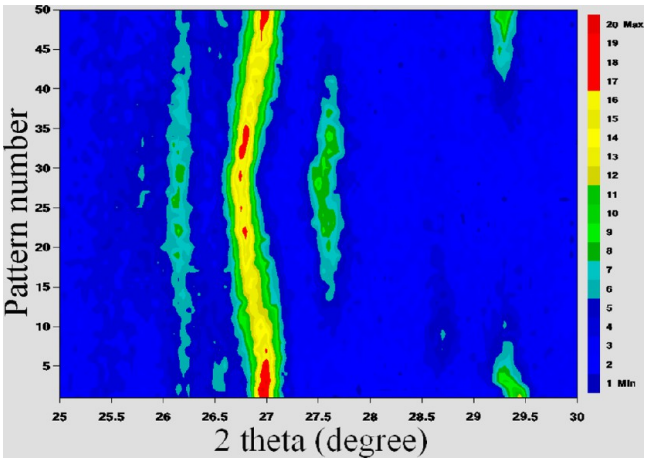

Figure 5. Image of change in intensity vs 2 theta in in situ XRD patterns of $LiVPO_4F$ cycled in 1.0−3.0 V.

Table 1. Lattice Parameters of $LiVPO_4F$ and $Li_4Ti_5O_{12}$ in Different Lithiation and Delithiation States

sample	space group	*a* (Å)	*b* (Å)	*c* (Å)	*V* (Å^3)
$LiVPO_4F$	*P*-1	5.1746	5.3091	7.2512	174.337
Li_2VPO_4F	*C*2/*c*	7.2265	7.9453	7.3086	374.231
Li_3VPO_4F	*C*2/*c*	7.2185	7.9396	7.3013	373.011
$Li_4Ti_5O_{12}$	$Fd\bar{3}m$	8.3562	8.3562	8.3562	583.481
$Li_7Ti_5O_{12}$	$Fd\bar{3}m$	8.3523	8.3523	8.3523	582.664
$Li_{8.5}Ti_5O_{12}$	$Fd\bar{3}m$	8.3456	8.3456	8.3456	581.263

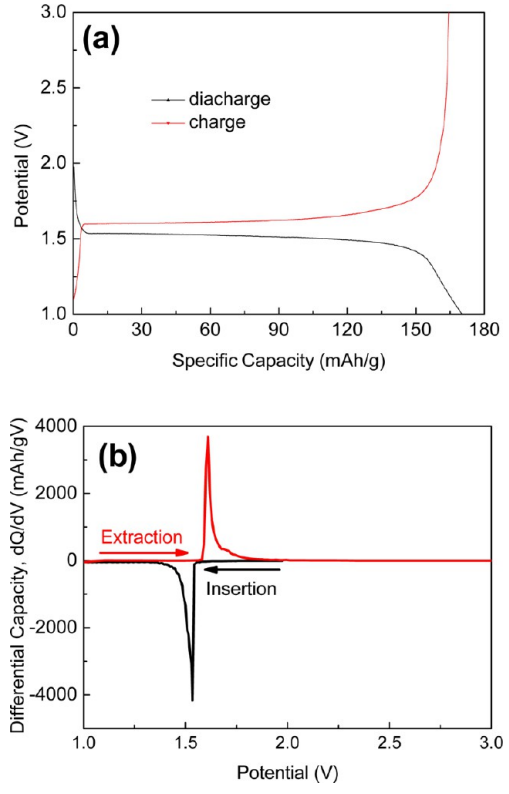

Figure 6. (a) Initial galvanostatic charge/discharge curves and (b) differential capacity profile of $Li_4Ti_5O_{12}$ cycled in 1.0−3.0 V.

according to Gibbs phase rule.[27] The lithium insertion/extraction reaction for $Li_4Ti_5O_{12}$ can be summarized as[28]

$$Li_{3(8a)}[]_{(16c)}[LiTTi_5^{4+}]_{(16d)}O_{12(32e)} + 3Li^+ + 3e^- \leftrightarrow []_{(8a)}Li_{6(16)c}[LiTi_3^{3+}Ti_2^{4+}]_{(16d)}O_{12(32e)} \quad (3)$$

On the basis of eq 3, a theoretical capacity of 175 mA h/g can be delivered corresponding to 3.0 Li uptake per formula. However, the initial reversible specific capacity of $Li_4Ti_5O_{12}$ is

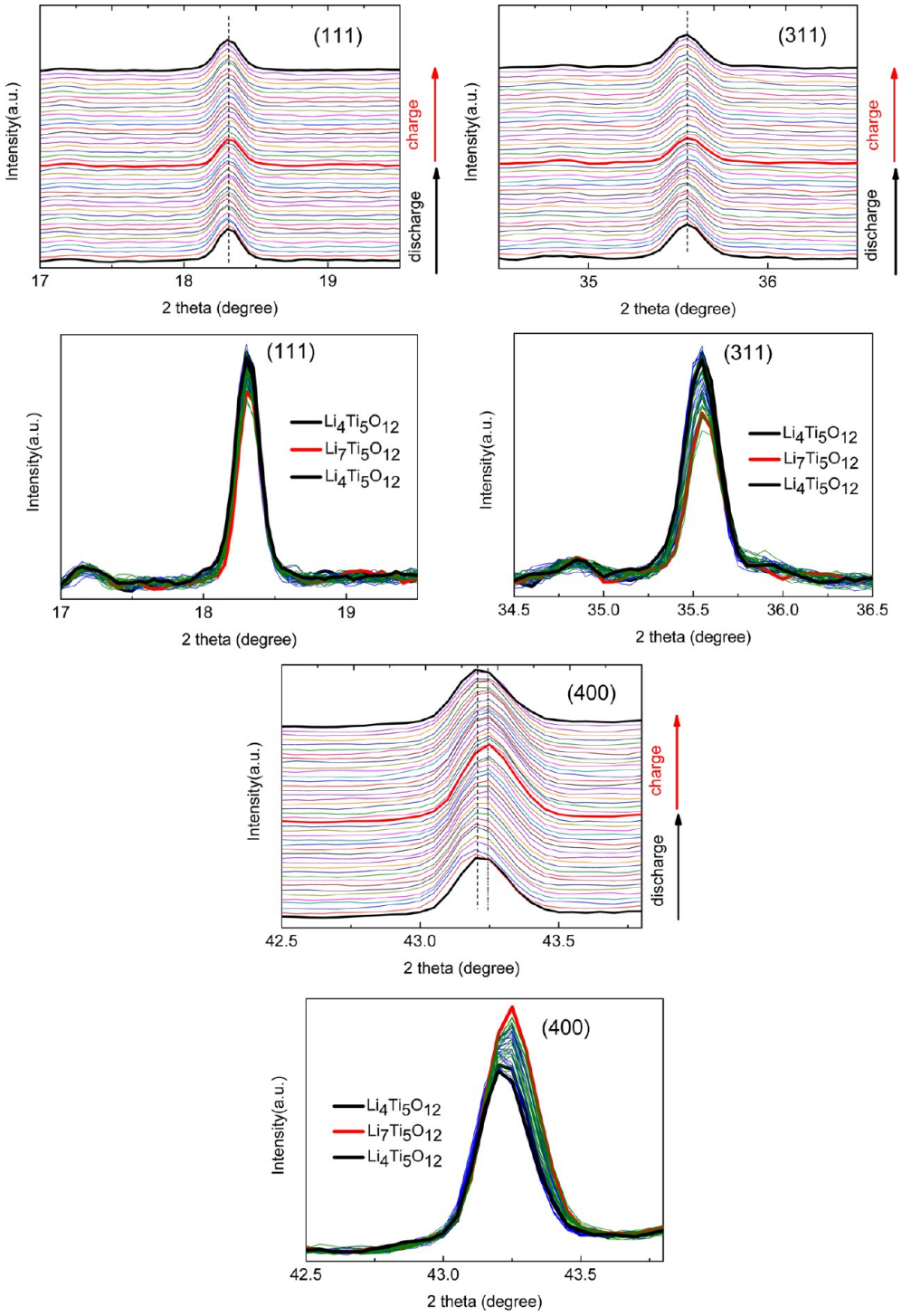

Figure 7. In situ XRD patterns during the first charge/discharge process of $Li_4Ti_5O_{12}$ cycled in 1.0−3.0 V.

164.5 mAh/g in 1.0−3.0 V corresponding to 2.82 Li per formula extraction from $Li_7Ti_5O_{12}$ during recharge, as seen in Figure 6a. This is due to the occurrence of irreversible lithium insertion in the structure. The initial Coulombic efficiency of $Li_4Ti_5O_{12}$ is up to 96.7% and higher than that (79.8%) of $LiVPO_4F$, which may be due to the characteristics of zero structural strain of spinel $Li_4Ti_5O_{12}$ during lithium insertion/extraction reaction. The differential capacity profile of $Li_4Ti_5O_{12}$ in Figure 6b shows that the discharge/charge process is characterized by a couple of differential capacity peaks at around 1.53 and 1.61 V, which indicates the high degree reversible electrochemical reaction between $Li_4Ti_5O_{12}$ and $Li_7Ti_5O_{12}$ when the amount of inserted lithium ions is limited within three per formula.

As reported, the amount of lithium atoms at tetrahedral 8a sites or octahedral 16c sites in the spinel $Li_4Ti_5O_{12}$ structure reflects upon the relative intensities of XRD patterns, especially for the (111), (311) and (400) planes.[11] Viewed from the in situ XRD data in Figure 7 and Figure S3 in the Supporting Inforamtion, we failed to observe the shift of characteristic diffraction peaks. It indicates that $Li_4Ti_5O_{12}$ not only possesses high structural stability but also shows similar/same structure with lithiated $Li_{4+x}Ti_5O_{12}$ during the insertion/extraction

dx.doi.org/10.1021/am402132u | ACS Appl. Mater. Interfaces 2013, 5, 8615−8627

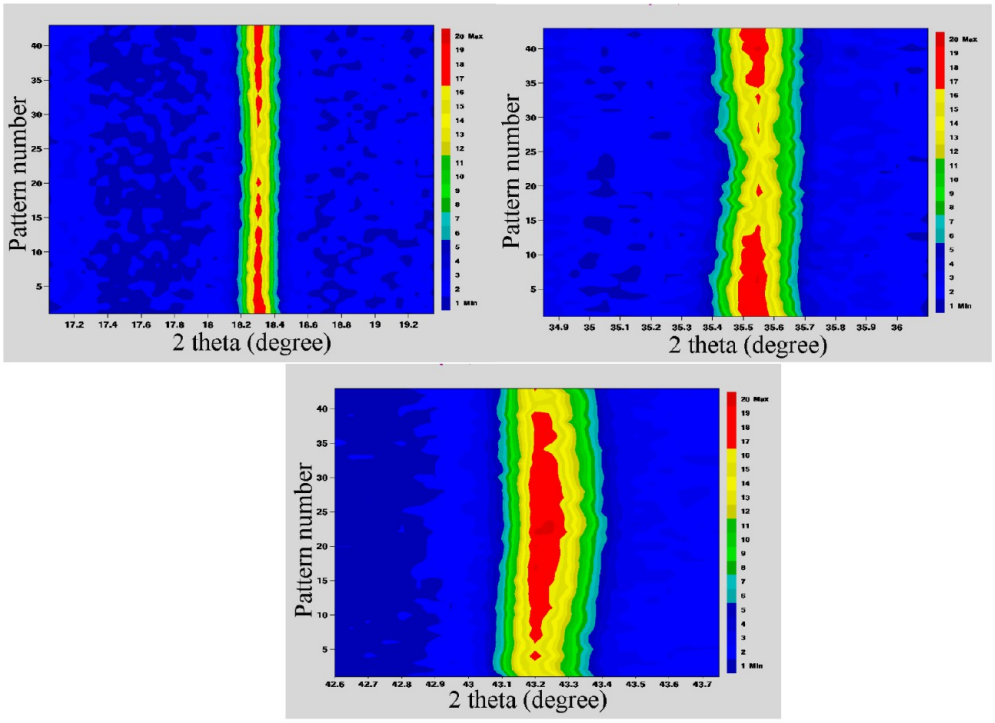

Figure 8. Image of change in intensity vs 2θ in in situ XRD patterns of $Li_4Ti_5O_{12}$ cycled in 1.0−3.0 V.

process. The Rietveld refinement of XRD from lithiated $Li_7Ti_5O_{12}$ is carried out and the atomic positions are listed in Table S4. Wagemaker ever reported that the overall variation of the lattice parameters of $Li_4Ti_5O_{12}$ during the insertion/extraction process is 0.07% with lattice parameter a changing from 8.3595 to 8.3538 Å.[29] Here, the whole volume change between $Li_4Ti_5O_{12}$ (583.481 Å^3) and $Li_7Ti_5O_{12}$ (582.664 Å^3) is merely 0.14% during cycling in 1.0−3.0 V, as shown in Table 1. Besides, the reversible change in intensity vs 2 theta of in situ XRD patterns also demonstrates the reversible structural evolution between $Li_4Ti_5O_{12}$ and $Li_7Ti_5O_{12}$ as shown in Figure 8. The relative intensity and fwhm value of the diffraction peak at 35.627° (corresponding to (311) plane) decrease with a discharge process to 1.0 V and reversibly recover after a recharge process to 3.0 V. For comparison, the relative intensity and fwhm value of the diffraction peak at 43.25° (corresponding to (400) plane) increase with a discharge process to 1.0 V and reversibly recover after a recharge process to 3.0 V. As shown by electrochemical behaviors and in situ XRD patterns, the phase transition of $Li_4Ti_5O_{12}$ from spinel to rock-salt structure is highly reversible and this compound will be energy favorable as high power anode materials.

Viewed from eq 3, we can find that there are two remained tetravalent titanium ions (40% of all titanium ions) in the reduction product $Li_7Ti_5O_{12}$, which can accept electrons to be reduced to form probably final product $Li_9Ti_5O_{12}$. Therefore, another 2.0 Li per formula could be intercalated into $Li_7Ti_5O_{12}$ if there are enough interstitial sites in $Li_7Ti_5O_{12}$. Based on the above analysis, it is necessary to study the electrochemical properties and structural evolutions in a broader electrochemical window (0.0−3.0 V). Besides, the study of the reaction behavior of anode materials during depth discharge is significant for the safety issues of lithium-ion batteries.

Figure 9 illustrates the initial galvanostatic charge/discharge curves of $Li_4Ti_5O_{12}$ cycled in 0.0−3.0 V. We observe that

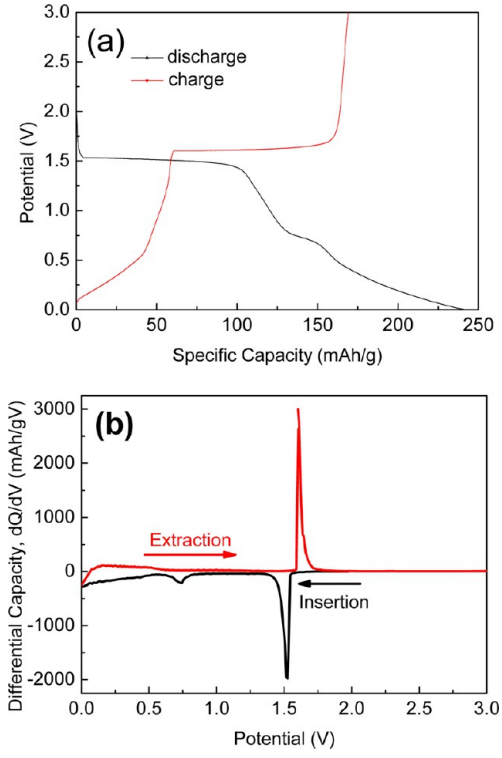

Figure 9. (a) Initial galvanostatic charge/discharge curves and (b) differential capacity profile of $Li_4Ti_5O_{12}$ cycled in 0.0−3.0 V.

$Li_4Ti_5O_{12}$ exhibits one flat potential plateau at around 1.52 V and three slopes below 1.0 V during insertion when the low cutoff potential is 0.0 V, corresponding to a discharge capacity of 241.4 mA h/g. Upon extraction, the slope at 0.75 V disappears, two other slopes (0.0−0.6 V and 0.6−1.5 V) shorten and a reversible flat delithiation plateau at 1.61 V is observed, which are

dx.doi.org/10.1021/am402132u | ACS Appl. Mater. Interfaces 2013, 5, 8615−8627

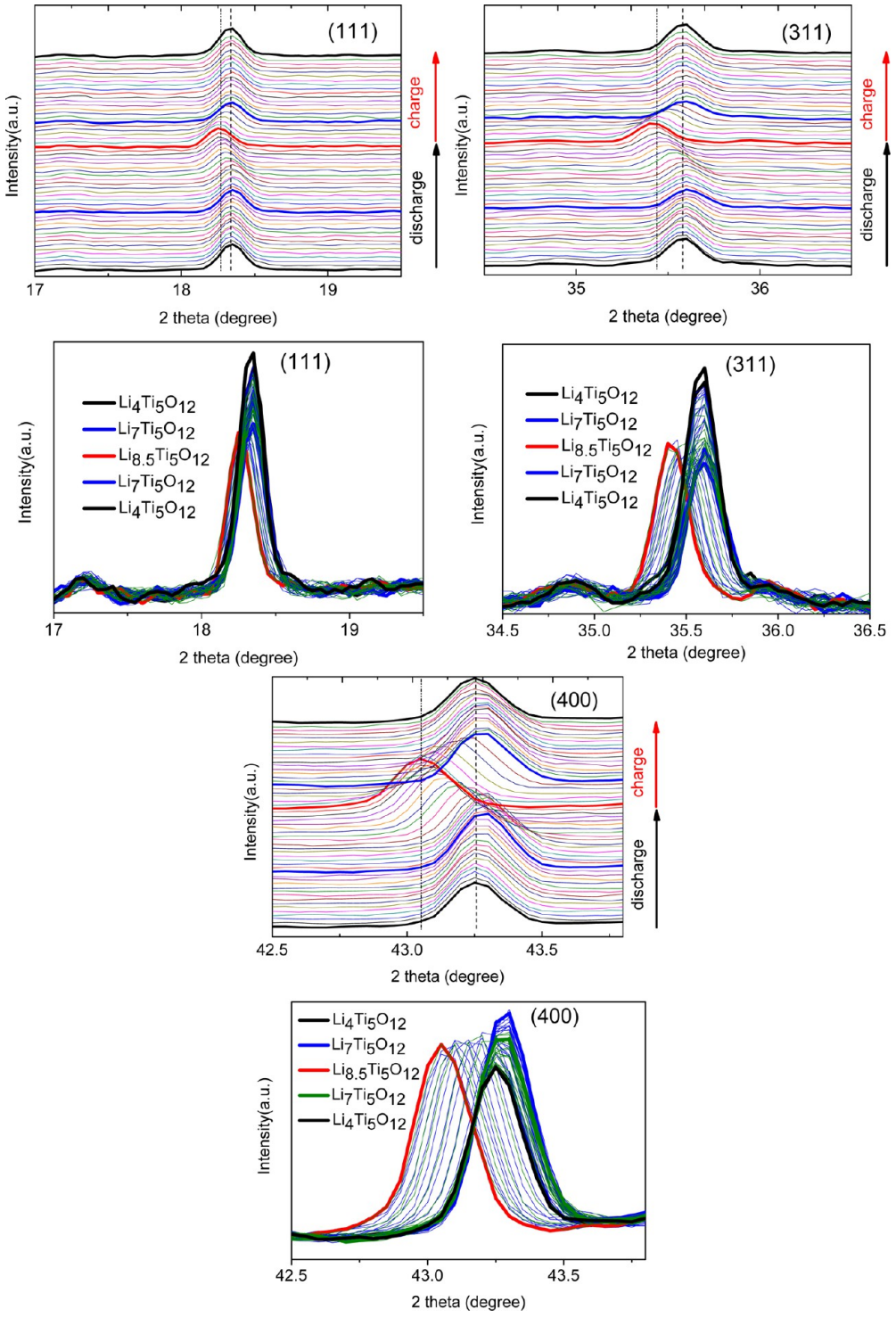

Figure 10. In situ XRD patterns during the first charge/discharge process of $Li_4Ti_5O_{12}$ cycled in 0.0−3.0 V.

corresponding to a recharge capacity of 174.3 mAh/g. The first Coulombic efficiency of $Li_4Ti_5O_{12}$ is 72.2%, which is far lower that (96.7%) of $Li_4Ti_5O_{12}$ when the low cutoff potential is 1.0 V. This is mainly due to the formation of solid electrolyte interphase (SEI) film on the surface of $Li_4Ti_5O_{12}$ during the initial electrochemical process in this broad potential window, which consumes part of inserted lithium ions as reported by Shu.[30] The differential capacity profile of $Li_4Ti_5O_{12}$ in Figure 9b presents an irreversible reduction peak at around 0.73 V, which is in good agreement with the electrolyte irreversible reduction decomposition to form SEI film below 1.0 V and probable irreversible structural transformation. In brief, $LiVPO_4F$ and $Li_4Ti_5O_{12}$ electrode are indeed SEI layer free materials in the electrochemical window between 1.0 and 3.0 V.

Observed from Figure 9a, we can find that $Li_4Ti_5O_{12}$ shows obvious capacity loss in the three slopes and no capacity loss in the potential plateau at around 1.55 V when it is discharged to 0.0 V. With the descending of the low cutoff potential from 1.0 to 0.0 V, the insertion capacity is increased to 241.4 mAh/g and extra 110 mAh/g can be obtained below 1.0 V, which indicates that

dx.doi.org/10.1021/am402132u | ACS Appl. Mater. Interfaces 2013, 5, 8615−8627

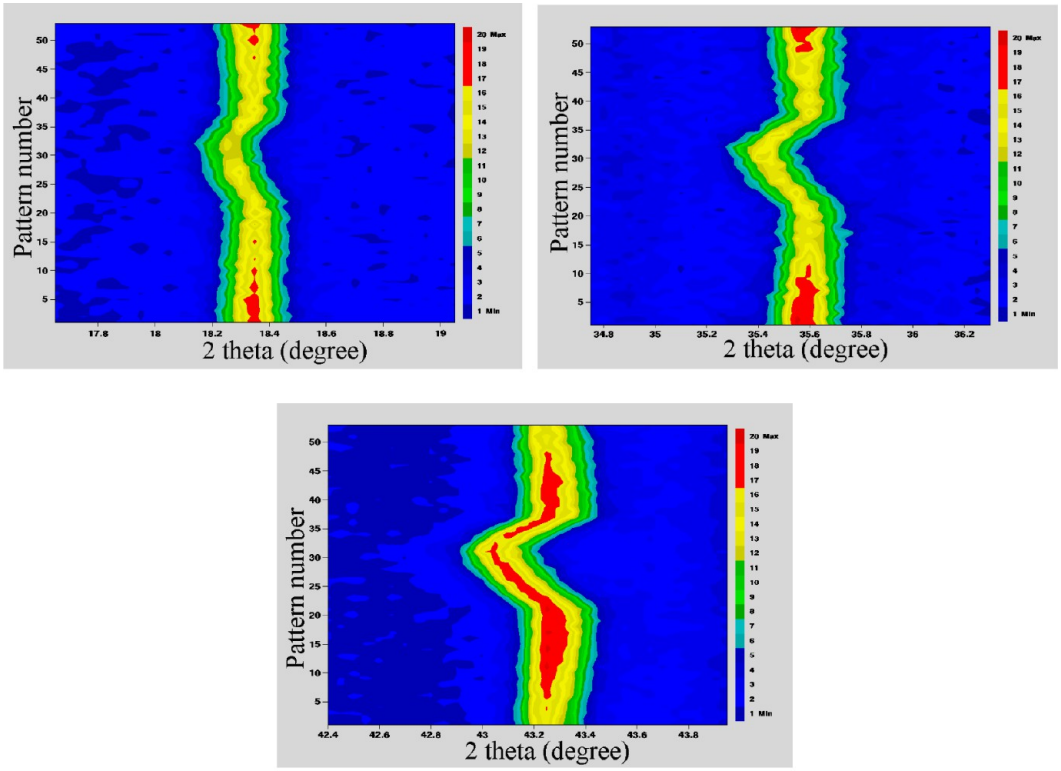

Figure 11. Image of change in intensity of 2θ in in situ XRD patterns of $Li_4Ti_5O_{12}$ cycled in 0.0−3.0 V.

lithium ion can further intercalate into the structure of $Li_4Ti_5O_{12}$ at low potential. Except for the irreversible SEI film formation, the lithiation slopes between 1.2 and 0.0 V indicate the occupation of lithium ions in two types of sites with different energies, besides 16*c* sites. Therefore, more than three lithium ions can further insert into the 8*a*, 8*b*, and 48*f* sites. Whether 8*a* or 8*b* sites are occupied during lithium insertion, the insertion/extraction process will not be interfered owing to the equivalent environment of 8*a* and 8*b* sites. In contrast, the capacity fading during cycling in 0.0−3.0 V is resulted from the lithium ions occupying 48*f* sites, which is electrochemically irreversible.[31]

Compared with the two-phase mechanism at 1.55 V, the appearance of three slopes below 1.2 V indicates the appearance of new electrochemical insertion process for $Li_4Ti_5O_{12}$. Yao ever reported an additional slope at around 0.75 V with the explanation of a core/shell structure model and carbon-triggered capacity effect.[32] However, Cho pointed that the slope at 0.75 V gradually elongated with the increase of the particle size.[33] They considered that the slope separation during discharge was mainly originated from the lithium ion diffusion kinetics, which are related to the particle size rather than the formation of an intermediate phase in $Li_4Ti_5O_{12}$ system. Borghols also reported the size effects on the electrochemical behavior of $Li_{4+x}Ti_5O_{12}$ spinel and considered the origin of the slope is related to the particle size.[34] In this paper, the size of $Li_4Ti_5O_{12}$ particles is about 0.5 μm. Consequently, submicro-$Li_4Ti_5O_{12}$ particles may also have high reactivity for lithium ions insertion at the surface and bulk of $Li_4Ti_5O_{12}$, which partially results in the appearance of the slope at 0.75 V. Ganapathy reported that the occupation of 8*a* sites in the structure allows the lithium storage capacity of submicro-$Li_7Ti_5O_{12}$ far exceed that of bulk $Li_7Ti_5O_{12}$ at a potential below 1.0 V when the 16*c* sites are fully occupied.[35] Therefore, the lithium insertion/extraction reaction for $Li_4Ti_5O_{12}$ below 1.0 V can be summarized as:[31]

$$[]_{(8c)}Li_{6(16c)}[LiTi_3^{3+}Ti_2^{4+}]_{(16d)}O_{12(32e)} + 2e^- + 2Li^+ \leftrightarrow Li_{2(8a)}Li_{6(16c)}[LiTi_5^{3+}]_{(16d)}O_{12(32e)} \quad (4)$$

As seen in eq 4, all the Ti^{4+} in $Li_4Ti_5O_{12}$ is totally reduced to Ti^{3+} after a discharge process to 0.0 V. $Li_4Ti_5O_{12}$ could deliver a theoretical capacity of 292 mAh/g according to the reduction of all the Ti^{4+} in the compound. Ge reported that the spinel $Li_4Ti_5O_{12}$ can accommodate 5 mol lithium ions per formula and its theoretical capacity is limited by the number of Ti^{4+} not the 8a and 16c sites when it is discharged to 0.0 V.[28] However, Zhong considered that $Li_7Ti_5O_{12}$ could not transform into $Li_9Ti_5O_{12}$ but could transform into quasi rock-salt $Li_{8.5}Ti_5O_{12}$ when it is discharged to 0.0 V according to the first principle calculation.[36] Because the predicted intercalation potential will become negative when lithium ions further insert into $Li_{8.5}Ti_5O_{12}$. Consequently, the valence of Ti in the compound should be a couple of 3+ and 4+ when $Li_4Ti_5O_{12}$ is discharged to 0.0 V. Therefore, the theoretical capacity of $Li_4Ti_5O_{12}$ is limited neither the number of tetravalent titanium ions nor the octahedral/tetrahedral sites to accommodate lithium ions.

Based on the above analysis, we adopt in situ XRD technology to study the insertion/extraction mechanism of $Li_4Ti_5O_{12}$ in 0.0−3.0 V, as shown in Figure 10 and Figure S4 in the Supporting Information. The diffraction peaks at 18.37, 35.63, and 62.88° respectively reflecting the characteristic (111), (311), and (400) planes do not shift during a discharge process from 3.0 to 1.0 V and a reverse charge process from 1.0 to 3.0 V, which is consistent with the above results in 1.0−3.0 V. However, all these three diffraction peaks gradually shift to low angles during a discharge process from 1.0 to 0.0 V and then they return reversibly to their original Bragg positions when it is charged up to 1.0 V. The peak shifting is attributed to Li^+ insertion into $Li_4Ti_5O_{12}$ by a two-step process. The Bragg positions of characteristic diffraction peaks

dx.doi.org/10.1021/am402132u | ACS Appl. Mater. Interfaces 2013, 5, 8615−8627

are maintained when lithium ions just diffuse from 8*a* to 16*c* sites in the lattice with a discharge process to 1.0 V and the shift of Bragg positions occurs with some lithium ions further insertion until 0.0 V, corresponding to the lithium-ion occupation of 8*a* sites in $Li_7Ti_5O_{12}$ to form $Li_{8.5}Ti_5O_{12}$, which is similar to that reported by Cho.[33] The Rietveld refinement of XRD from phase $Li_{8.5}Ti_5O_{12}$ is carried out and the atomic positions are listed in Table S5 in the Supporting Information. With the further occupation of 8*a* sites, the structural evolution of $Li_{7+x}Ti_5O_{12}$ below 1.0 V is a solid-solution single-phase mechanism, which is also confirmed by the lithiation/delithiation slopes between 0.0 and 1.0 V. These results are in a very visible degree of uniformity with the changes in intensity vs 2 theta in in situ XRD patterns as illustrated in Figure 11. Based on results in Table 1, it is clear that the volume variation between $Li_4Ti_5O_{12}$ (583.481 Å^3) and $Li_{8.5}Ti_5O_{12}$ (581.263 Å^3) is only 0.38%, which proves its zero-strain structural stability in a broad electrochemical window (0.0−3.0 V).

To closely compare the structural evolutions of $LiVPO_4F$ to that of $Li_4Ti_5O_{12}$, Figure 12 illustrates the initial galvanostatic

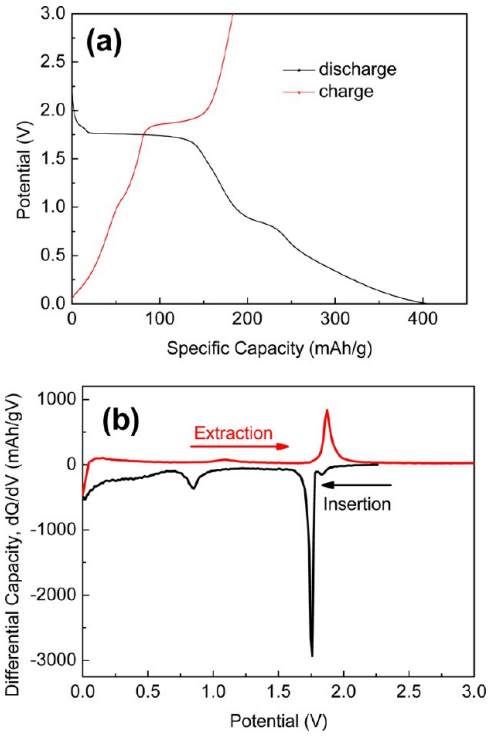

Figure 12. (a) Initial galvanostatic charge/discharge curves and (b) differential capacity profile of $LiVPO_4F$ cycled in 0.0−3.0 V.

charge/discharge curves of $LiVPO_4F$ cycled at 10 mA/g in the same potential window (0.0−3.0 V). It can be observed that $LiVPO_4F$ also exhibits one flat plateau at around 1.75 V and three slopes (0.0−0.5 V, 0.5−0.9 V and 0.9−1.5 V) between 1.5 and 0.0 V during insertion, which is similar with that revealed by $Li_4Ti_5O_{12}$. Upon extraction, the characteristic plateau and all the slopes shorten, which are different with those of $Li_4Ti_5O_{12}$, especially for the existence of slope at 0.78 V. To further observation, it can be found that the total insertion capacity increases to the value of 404.5 mAh/g with a discharge process to 0.0 V and extra 220 mA h/g can be obtained below 1.0 V, which indicates that additional lithium ion can intercalate the structure of Li_2VPO_4F at low potential. Therefore, it is thought that another 1.0 mol lithium ions per formula could be intercalated into Li_2VPO_4F when the cutoff potential is 0.0 V. The lithium insertion/extraction reaction for $LiVPO_4F$ in 0.0−1.0 V can be summarized as

$$Li_2V^{2+}PO_4F + Li^+ + e^- \leftrightarrow Li_3V^+PO_4F \quad (5)$$

The whole lithium insertion/extraction reaction for $LiVPO_4F$ in 0.0−3.0 V can be summarized as

$$LiV^{3+}PO_4F + 2Li^+ + 2e^- \leftrightarrow Li_3V^+PO_4F \quad (6)$$

Based on eq 6, a theoretical capacity of 312 mA h/g can be delivered corresponding to 2.0 Li uptake per formula. However, the initial discharge capacity of $LiVPO_4F$ is up to 404.5 mA h/g. It is thought that the extra lithiation capacity results from the electrolyte irreversible reduction decomposition to form SEI film below 1.0 V. In addition, the charge capacity of $LiVPO_4F$ is only 183.7 mA h/g, which is due to the occurrence of irreversible lithium insertion into the crystal structure and the consumption for the irreversible formation of SEI film. The formation of SEI film and dead lithium in the structure in the initial discharge process results in much lower Coulombic efficiency (45.4%) than that (79.8%) of $LiVPO_4F$ in a narrow working window (1.0−3.0 V). The differential capacity profile of $LiVPO_4F$ in Figure 12b presents a partial-irreversible differential capacity peak at 0.85 V, which is in good agreement with the electrolyte irreversible reduction decomposition to form SEI film besides the differential capacity peak at 1.75 V.

Viewed from the in situ XRD data of $LiVPO_4F$ cycled in 0.0−3.0 V in Figure 13 and Figure S5 in the Supporting Information, we find that the whole variation tendency of diffraction peaks in in situ XRD patterns is similar to that of $LiVPO_4F$ cycled in 1.0−3.0 V. It may be a fully reversible two-phase reaction in 1.0−3.0 V and a partial-reversible single-phase transition process below 1.0 V as the lithiation/delithiation plateau and slopes shown in Figure 12. All the feactured diffraction peaks of $LiVPO_4F$ gradually fade away during insertion, accompanied by the appearance of Bragg positions of Li_2VPO_4F. With further lithium ion insertion, some bragg positions, such as 26.7° and 27.5°, show slight shift to lower angles (26.6 and 27.4°). In the reverse charge process, almost no Bragg position shift can be observed when the sample is charged to 1.0 V. On the basis of the above results, it is known that the structure of Li_3VPO_4F is highly similar to that of Li_2VPO_4F, which presumably belongs to the space group *C*2/*c*. During lithium ion extraction, the featured diffraction peaks of Li_3VPO_4F disappear and the featured diffraction peaks of $LiVPO_4F$ reappear. However, the relative intensity of diffraction peaks can not return to the original values. It confirms the large irreversible capacity of $LiVPO_4F$ during the initial cycle in 0.0−3.0 V. These results are in a very degree of uniformity with the changes in intensity vs 2 theta in in situ XRD patterns as illustrated in Figure 14. Consequently, the in situ XRD data clearly demonstrate the biphasic reaction mechanism between $LiVPO_4F$ and Li_2VPO_4F, and the single-phase reaction mechanism between $LiVPO_4F$ and Li_3VPO_4F.

As anode material, it is also made a detailed comparison between $LiVPO_4F$ and $Li_4Ti_5O_{12}$ in terms of electrochemical performance. The charge−discharge curves of Li/$LiVPO_4F$ and Li/$Li_4Ti_5O_{12}$ cells at a current density of 10 mA/g cycled in 1.0−3.0 V and 0.0−3.0 V are shown in Figure 15. When the low cutoff potential is set at 1.0 V, the initial discharge and charge capacities of $LiVPO_4F$ are 167.3 and 131.9 mA h/g, which are close to the theoretical capacity (156 mA h/g) based on the electrochemical

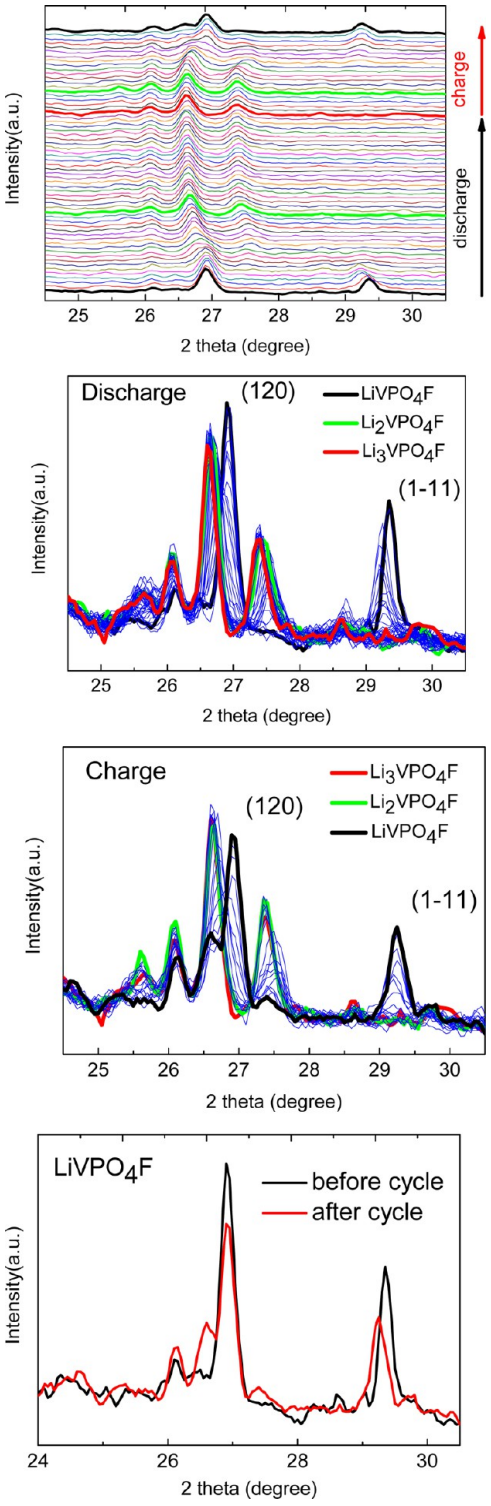

Figure 13. In situ XRD patterns during the first charge/discharge process of $LiVPO_4F$ cycled in 0.0−3.0 V.

reaction between $LiVPO_4F$ and Li_2VPO_4F, and the initial Coulombic efficiency is 79.8%. Seen from Figure 15b, it can be found that $LiVPO_4F$ could deliver the initial discharge and charge capacities of 701.7 and 273.4 mA h/g in 0.0−3.0 V, and the initial Coulombic efficiency decreases from 79.8 to 39.0%. After 20 cycles, the reversible capacities of $LiVPO_4F$ are 60.7 and 113.5 mA h/g with capacity retentions of 22.2 and 86.5% in the cycling potential ranges of 0.0−3.0 V and 1.0−3.0 V, respectively, as

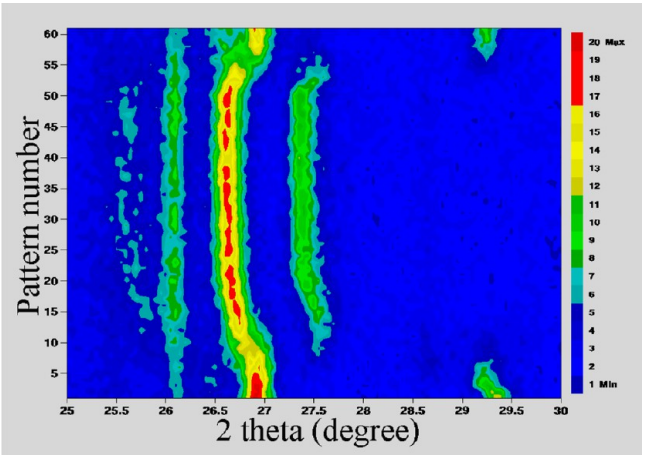

Figure 14. Image of change in intensity vs 2θ in in situ XRD patterns of $LiVPO_4F$ cycled in 0.0−3.0 V.

shown in panels a and b in Figure 15. It suggests that narrow cycling window is suitable for $LiVPO_4F$ to obtain outstanding cyclability.

In contrast, viewed from panels c and d in Figure 15, the initial discharge and charge capacities of $Li_4Ti_5O_{12}$ are 204.3 and 170.1 mA h/g, respectively, by cycling the material in 1.0−3.0 V. Corresponding initial Coulombic efficiency is 83.3%. With a discharge process to 0.0 V, it can be found that $Li_4Ti_5O_{12}$ could deliver the initial discharge and charge capacities of 438.3 and 306.5 mA h/g, respectively. The initial Coulombic efficiency greatly decreases from 83.3 to 69.9%. After 20 cycles, the reversible capacities of $Li_4Ti_5O_{12}$ are 179.2 and 167.1 mAh/g with capacity retentions of 58.5 and 98.2% in the cycling potential ranges of 0.0−3.0 and 1.0−3.0 V, respectively. The capacity loss may be due to electrolyte irreversible decomposition and dead lithium in the structure resulted from the breakdown and agglomeration of pristine particles after repeated cycles. Furthermore, the disappearance of the slope at 0.82 V in the following cycles demonstrates the formation of SEI film in the initial discharge process. In conclusion, it can be found that both $LiVPO_4F$ and $Li_4Ti_5O_{12}$ cycled in 0.0−3.0 V exhibit much higher lithium storage capacities than those cycled in 1.0−3.0 V but both samples display worse cycle performance. To further investigation, we find that the cycle stability of $Li_4Ti_5O_{12}$ far exceeds that of $LiVPO_4F$ in the same electrochemical potential window (1.0−3.0 V and 0.0−3.0 V), which is attributed to the zero-strain structure of $Li_4Ti_5O_{12}$. The capacity retentions of $Li_4Ti_5O_{12}$ is as high as 98.2% after 20 cycles, which also suggests the host structure of $Li_4Ti_5O_{12}$ cycled in 1.0−3.0 V is retained upon repeated insertion/extraction processes.

Figure 16 illustrates the charge/discharge performance at different current densities and rate capabilities of $LiVPO_4F$ and $Li_4Ti_5O_{12}$ cycled in 1.0−3.0 and 0.0−3.0 V. As seen in panels a and b in Figure 16, a specific discharge capacity of 167.3 mA h/g is observed when $LiVPO_4F$ is discharged to 1.0 V at a current density of 10 mA/g and the specific discharge capacities decrease to the values of 79.2, 50.9, and 29.9 mAh/g at higher current densities of 20, 40, and 80 mA/g, respectively. Increased the charge/discharge current density to 160 mA/g, the electrode can only deliver a specific capacity of 19.1 mAh/g in 1.0−3.0 V and this value is about 11.4% of the capacity at a current density of 10 mA/g. For comparison, $LiVPO_4F$ shows worse electrochemical properties in a broader electrochemical window (0.0−3.0 V) as shown in Figure 16b, e. With a discharge to 0.0 V, $LiVPO_4F$ can

dx.doi.org/10.1021/am402132u | ACS Appl. Mater. Interfaces 2013, 5, 8615−8627

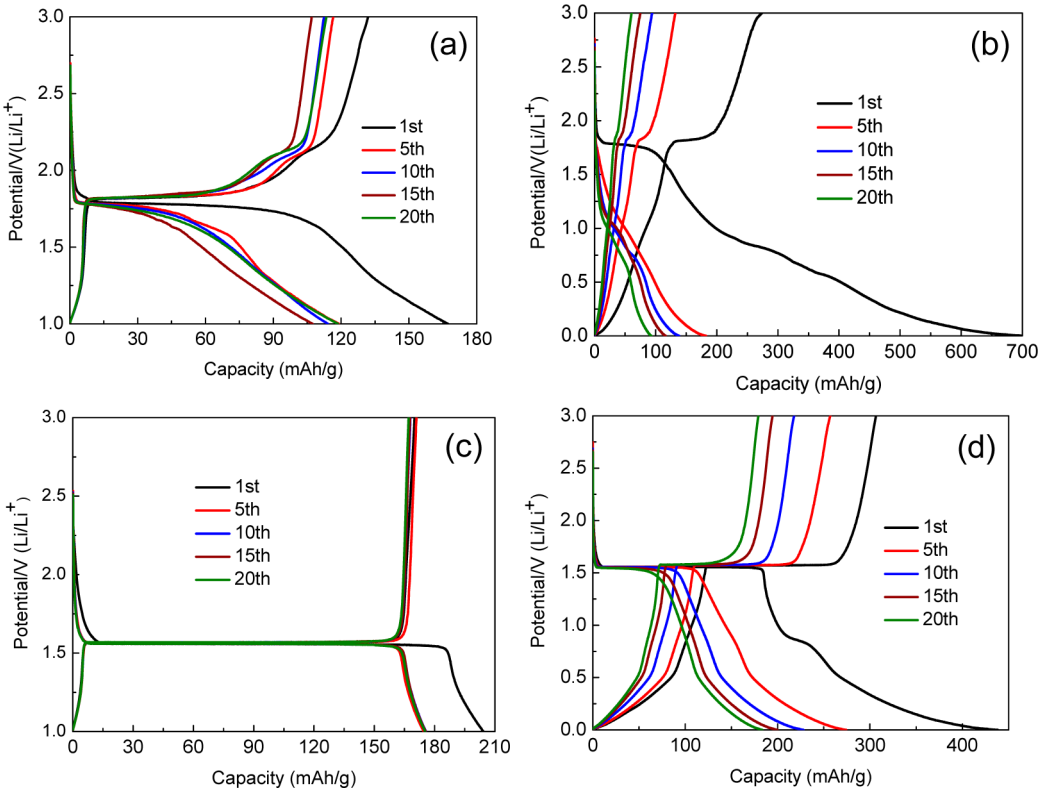

Figure 15. Charge/discharge curves of (a, b) Li/$LiVPO_4F$ and (c, d) Li/$Li_4Ti_5O_{12}$ cells at a current density of 10 mA/g. (a, c) 1.0−3.0 V; (b, d) 0.0−3.0 V.

deliver a huge discharge capacity of 701.7 mA h/g at a current density of 10 mA/g, but the initial discharge capacities reduce to 55.8, 30.4, 20.8, and 13.8 mA h/g at the current densities of 20, 40, 80, and 160 mA/g, respectively. They are much lower than those of $LiVPO_4F$ cycled in 1.0−3.0 V at the same current densities. To distinctly illustrate this result, the rate capability of $LiVPO_4F$ cycled in 1.0−3.0 V and 0.0−3.0 V is shown in Figure 16e, which indicates that $LiVPO_4F$ cycled in 1.0−3.0 V has better rate performance than that of $LiVPO_4F$ in 0.0−3.0 V. It is proved by the in situ XRD patterns as shown in Figures 4 and 13.

Seen from panels c and d in Figure 16, it can be observed that a specific discharge capacity of 204.3 mA h/g is delivered when $Li_4Ti_5O_{12}$ is discharged to 1.0 V at a current density of 10 mA/g and the lithium storage capacities can be maintained at 170.3, 165.1, and 153.3 mAh/g by using higher current densities of 20, 40, and 80 mA/g, respectively. Even using a charge/discharge current density as high as 160 mA/g, the electrode can still deliver a specific capacity of 131.7 mA h/g and this value is about 64.5% of the capacity obtained at a current density of 10 mA/g. For comparison, $Li_4Ti_5O_{12}$ with a discharge to 0.0 V can deliver a discharge capacity of 438.2 mA h/g at a current density of 10 mA/g, and the initial lithium storage capacities reduce to 169.9, 147.5, 114.2, and 64.6 mA h/g at higher current densities of 20, 40, 80, and 160 mA/g, respectively, which are slightly lower than those of $Li_4Ti_5O_{12}$ cycled in 1.0−3.0 V at the same current densities. To distinctly illustrate this result, the rate capability of $Li_4Ti_5O_{12}$ cycled in 1.0−3.0 V and 0.0−3.0 V is shown in Figure 16f. It can be seen that $Li_4Ti_5O_{12}$ cycled in 1.0−3.0 V has better rate performance than that of $Li_4Ti_5O_{12}$ in 0.0−3.0 V. Besides, it is obvious that the specific discharge capacity at the 1.55 V plateau of $Li_4Ti_5O_{12}$ cycled in 0.0−3.0 V decreases quickly with the increase of current density, which is similar to that reported by Yao,[32] and it confirms the characteristics of the kinetics control and the carbon-triggered capacity effect of the discharge potential profile for $Li_4Ti_5O_{12}$. However, the electrochemical charge/discharge curves of $Li_4Ti_5O_{12}$ cycled in 0.0−3.0 V at different current densities show similar shapes and behaviors. It can be also found that the capacity fading of $Li_4Ti_5O_{12}$ is much lower than that of $LiVPO_4F$ with the increase in the current density from 10 to 160 mA/g. It suggests that the rate performance of $Li_4Ti_5O_{12}$ far exceeds that of $LiVPO_4F$ in the same electrochemical potential window, which is probably attributed to the zero-strain characteristics of $Li_4Ti_5O_{12}$.

4. CONCLUSIONS

In the whole insertion/extraction process, $LiVPO_4F$ goes through reversible two-phase reaction between the two end-member phases $LiVPO_4F$ (*P*-1) and Li_2VPO_4F (*C*2/*c*) in 1.0−3.0 V, and Li_2VPO_4F transforms to Li_3VPO_4F (*C*2/*c*) with a depth discharge process to 0.0 V. Additionally, $Li_4Ti_5O_{12}$ experiences through reversible a two-phase reaction between the two end-member phases $Li_4Ti_5O_{12}$ (spinel) and $Li_7Ti_5O_{12}$ (rock-salt) in 1.0−3.0 V, and $Li_7Ti_5O_{12}$ transforms to $Li_{8.5}Ti_5O_{12}$ (quasi rock-salt) phase with a depth discharge to 0.0 V. According to the in situ XRD patterns, high degree reversible structure changes are observed for $Li_4Ti_5O_{12}$, proving its high structure stability during the charge/discharge process. In contrast, slight irreversibility in structural evolution can be detected for $LiVPO_4F$. As a result, the cycle and rate performances of $Li_4Ti_5O_{12}$ far exceed those of $LiVPO_4F$ in the same electrochemical potential window (1.0−3.0 and 0.0−3.0 V). In particular, the capacity retentions of $Li_4Ti_5O_{12}$ cycled in 1.0−3.0 V is as high as 98.2% after 20 cycles. Therefore, $Li_4Ti_5O_{12}$ is expected to be the candidate anode material

dx.doi.org/10.1021/am402132u | ACS Appl. Mater. Interfaces 2013, 5, 8615−8627

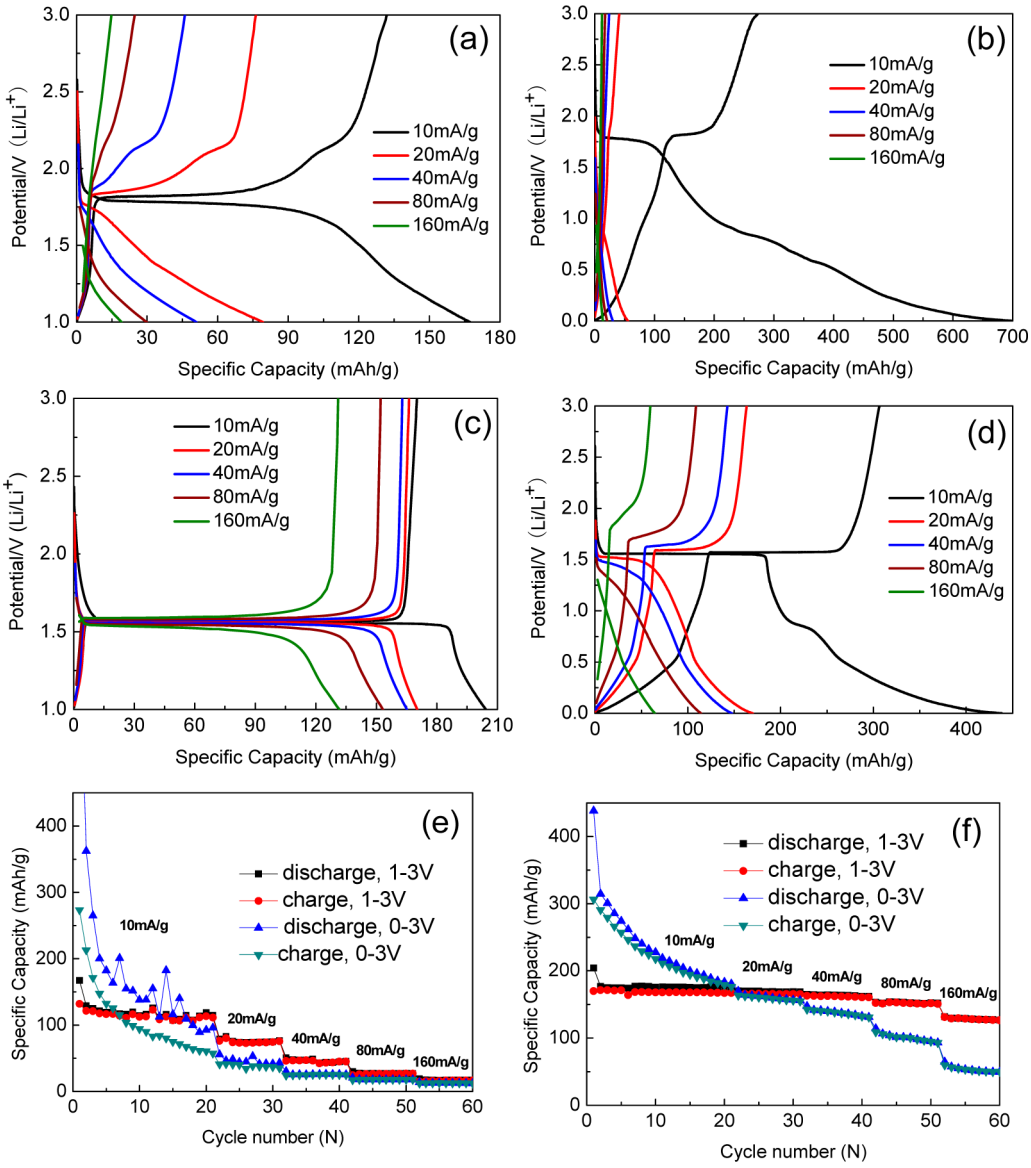

Figure 16. Charge/discharge curves of (a, b) $LiVPO_4F$ and (c, d) $Li_4Ti_5O_{12}$ at different current densities and corresponding rate capabilities of (e) $LiVPO_4F$ and (f) $Li_4Ti_5O_{12}$.

considering its high operating potential, structural zero-strain property and excellent cycle stability and rate performance.

■ ASSOCIATED CONTENT

Supporting Information

Tables S1−S5 show the structural parameters of $LiVPO_4F$, $Li_4Ti_5O_{12}$, Li_2VPO_4F, $Li_7Ti_5O_{12}$, and $Li_{8.5}Ti_5O_{12}$. Figure S1 shows the HRTEM images of $LiVPO_4F$ and $Li_4Ti_5O_{12}$ powders. Figures S2−S5 show the in situ XRD patterns of $Li_4Ti_5O_{12}$ and $LiVPO_4F$ cycled in different working potential windows. This material is available free of charge via the Internet at http://pubs.acs.org/.

■ AUTHOR INFORMATION

Corresponding Author

*E-mail: sergio_shu@hotmail.com or shujie@nbu.edu.cn. Tel: +86-574-87600787. Fax: +86-574-87609987.

Notes

The authors declare no competing financial interest.

■ ACKNOWLEDGMENTS

This work is sponsored by National 863 Program (2013AA050901), National Natural Science Foundation of China (51104092 and 61078055) and Qianjiang Talent Project of Zhejiang Province (2011R10089). The work is also supported by K. C. Wong Magna Fund in Ningbo University, Open Foundation of State Key Laboratory of Materials Processing and Die & Mold Technology (2012-P01), Open Foundation of State Key Laboratory of Electronic Thin Films and Integrated Devices (KFJJ201209) and Open Foundation of State Key Laboratory Breeding Base of Green Chemistry-Synthesis Technology (GCTKF2012002).

■ REFERENCES

(1) Scrosati, B. *Nature* **1995**, *373*, 557−558.
(2) Armand, M.; Tarascon, J. M. *Nature* **2008**, *451*, 652−657.
(3) Tarascon, J. M.; Armand, M. *Nature* **2001**, *414*, 359−367.
(4) Scosati, B.; Garche, J. *J. Power Sources* **2010**, *195*, 2419−2430.
(5) Yi, T. F.; Xie, Y.; Zhu, Y. R.; Zhu, R. S.; Shen, H. Y. *J. Power Sources* **2013**, *222*, 448−454.

(6) Shin, J. W.; Chung, K. Y.; Ryu, J. H.; Park, I. W.; Yoon, D. H. *Appl. Phys. A Mater* **2012**, *107*, 769−775.
(7) Barker, J.; Gover, R. K. B.; Burns, P.; Bryan, A. J. *Electrochem. Solid-State Lett.* **2007**, *10*, A130−A133.
(8) Yang, L.; Chen, J. Z.; Tang, Y. F.; Fang, S. H. *Prog. Chem.* **2011**, *23*, 310−317.
(9) Ouyang, C. Y.; Zhong, Z. Y.; Lei, M. S. *Electrochem. Commun.* **2007**, *9*, 1107−1112.
(10) Ge, H.; Li, N.; Li, D. Y.; Dai, C. S.; Wang, D. L. *Electrochem. Commun.* **2008**, *10*, 719−722.
(11) Ohzuku, T.; Ueda, A.; Yamamoto, N. *J. Electrochem. Soc.* **1995**, *142*, 1431−1435.
(12) Barker, J.; Gover, R. K. B.; Burns, P.; Bryan, A. *Electrochem. Solid-State Lett.* **2005**, *8*, A285−A287.
(13) Mba, J. M. A.; Croguennec, L.; Basir, N. I.; Barker, J.; Masquelier, C. *J. Electrochem. Soc.* **2012**, *159*, A1171−A1175.
(14) Mba, J. M. A.; Masquelier, C.; Suard, E.; Croguennec, L. *Chem. Mater.* **2012**, *24*, 1223−1234.
(15) Barker, J.; Saidi, M. Y.; Swoyer, J. L. *J. Electrochem. Soc.* **2003**, *150*, A1394−A1398.
(16) Ma, R.; Shu, J.; Hou, L.; Shui, M.; Shao, L. Y.; Wang, D. J.; Ren, Y. L. *Ionics* **2013**, *19*, 725−730.
(17) Shu, J.; Shui, M.; Xu, D.; Ren, Y. L.; Wang, D. J.; Wang, Q. C.; Ma, R.; Zheng, W. D.; Gao, S.; Hou, L.; Xu, J. J.; Cui, J.; Zhu, Z. H.; Li, M. *J. Mater. Chem.* **2012**, *22*, 3035−3043.
(18) Shu, J.; Shui, M.; Xu, D.; Gao, S.; Yi, T. F.; Wang, D. J.; Li, X.; Ren, Y. L. *Ionics* **2011**, *17*, 503−509.
(19) Barker, J.; Gover, R. K. B.; Burns, P.; Bryan, A.; Saidi, M. Y.; Swoyer, J. L. *J. Electrochem. Soc.* **2005**, *152*, A1776−A1779.
(20) Plashnitsa, L. S.; Kobayashi, E.; Okada, S.; Yamaki, J. *Electrochim. Acta* **2011**, *56*, 1344−1351.
(21) Zheng, J. C.; Zhang, B.; Yang, Z. H. *J. Power Sources* **2012**, *202*, 380−383.
(22) Ellis, B. L.; Ramesh, T. N.; Davis, L. J. M.; Goward, G. R.; Nazar, L. F. *Chem. Mater.* **2011**, *23*, 5138−5148.
(23) Ramesh, T. N.; Lee, K. T.; Ellis, B. L.; Nazar, L. F. *Electrochem. Solid-State Lett.* **2010**, *13*, A43−A47.
(24) Marx, N.; Croguennec, L.; Carlier, D.; Wattiaux, A.; Cras, F. L.; Suard, E.; Delmas, C. *Dalton Trans.* **2010**, *39*, 5108−5116.
(25) Rui, X. H.; Yesibolati, N.; Chen, C. H. *J. Power Sources* **2011**, *196*, 2279−2282.
(26) Davis, L. J. M.; Ellis, B. L.; Ramesh, T. N.; Nazar, L. F.; Bain, A. D.; Goward, G. R. *J Phys. Chem. C* **2011**, *115*, 22603−22608.
(27) Scharner, S.; Weppner, W.; Schmid-Beurmann, P. *J. Electrochem. Soc.* **1999**, *146*, 857−861.
(28) Ge, H.; Li, N.; Li, D. Y.; Dai, C. S.; Wang, D. L. *J. Phys. Chem. C* **2009**, *113*, 6324−6326.
(29) Wagemaker, M.; Simon, D. R.; Kelder, E. K.; Schoonman, J.; Ringpfeil, C.; Haake, U.; Lutzenkirchen-Hecht, D.; Frahm, R.; Mulder, F. M. *Adv. Mater.* **2006**, *18*, 3169−3173.
(30) Shu, J. *Electrochem. Solid-State Lett.* **2008**, *11*, A238−A240.
(31) Shu, J. *J. Solid State Electrochem.* **2009**, *13*, 1535−1539.
(32) Yao, X. L.; Xie, S.; Nian, H. Q.; Chen, C. H. *J. Alloys Comp.* **2008**, *465*, 375−379.
(33) Cho, W.; Song, J. H.; Park, M. S.; Kim, J. H.; Kim, J. S.; Kim, Y. J. *J. Electrochem. Sci. Tech.* **2010**, *1*, 85−91.
(34) Borghols, W. J. H.; Wagemaker, M.; Lafont, U.; Kelder, E. M.; Mulder, F. M. *J. Am. Chem. Soc.* **2009**, *131*, 17786−17792.
(35) Ganapathy, S.; Wagemaker, M. *Nano Lett.* **2012**, *6*, 8702−8712.
(36) Zhong, Z. Y.; Ouyang, C. Y.; Shi, S. Q.; Lei, M. S. *ChemPhysChem* **2009**, *9*, 2104−2108.